

Quadruple decomposition of current-dominated pulsatile rough-wall turbulent pipe flow

T. O. Jelly¹, R. C. Chin², S. J. Illingworth¹, J. P. Monty¹, I. Marusic¹ and A. S. H. Ooi¹

¹Department of Mechanical Engineering, University of Melbourne, Melbourne, Victoria, 3010, Australia

²School of Mechanical Engineering, University of Adelaide, Adelaide, South Australia 5005, Australia

Abstract

The physics of pulsatile rough-wall turbulent pipe flow is investigated using data from direct numerical simulation (DNS). Three geometrically-scaled sinusoidal roughness topographies are considered — the amplitude and wavelength of each surface are systematically varied whilst holding their amplitude-to-wavelength ratio constant. Pulsation is achieved by imposing a time-harmonic axial pressure gradient. The resulting flow-field is triple phase-averaged (in two spatial directions and also in time) which permits a quadruple decomposition of the instantaneous field variables to be invoked. The four components of the quadruple decomposition are: (i) a global-averaged mean component; (ii) a steady roughness-induced fluctuation; (iii) an unsteady pulsation-induced fluctuation and (iv) the remaining turbulent fluctuation. We compare statistics of (i)-(iv) against their non-pulsatile counterpart using past results from related work [1, 2]. Whilst the pulsatile and non-pulsatile data collapse well in the outer region, clear differences are observed in the near-roughness region. In particular, profiles of the mean axial velocity, roughness-induced stress and turbulence-induced stress exhibit consistently lower magnitudes below the roughness crests under pulsatile conditions.

Introduction

Pulsatile rough-wall flows appear regularly in nature and engineering. For example, the fluid dynamic properties of circulatory systems and rotating machinery are both strongly influenced by flow unsteadiness and surface roughness. Pulsating smooth-wall flows have been studied extensively under laminar [12], transitional [13] and fully-turbulent [9] conditions across a wide range of forcing parameters. Roughness effects are also well-documented in the context of steady pressure gradient turbulent flows [3]. In contrast, studies of pulsatile rough-wall turbulent flows remain scarce throughout the literature.

This study focuses on current-dominated (CD) pulsatile rough-wall turbulent pipe flow in the very-high-frequency (VHF) regime. In the absence of roughness, such a flow can be characterised by three non-dimensional parameters: (i) the friction Reynolds number, Re_τ ; (ii) the inner-scaled forcing frequency, ω^+ , and (iii) the ratio of the oscillating centre-line velocity to the bulk velocity, β . Parameters (i)-(iii) are defined here as

$$Re_\tau \equiv \frac{u_\tau R}{\nu}, \quad \omega^+ \equiv \frac{\omega \nu}{u_\tau^2}, \quad \beta \equiv \frac{U_o}{U_b} \quad (1)$$

where u_τ is the friction velocity, R is the pipe radius, ν is the kinematic viscosity, U_o is oscillating centre-line velocity and U_b is the bulk velocity.

The CD regime is attained when the ratio of the oscillating centre-line velocity to the bulk velocity is less than one ($\beta < 1$) [6]. The VHF regime is defined by the forcing frequency, ω^+ , and the Stokes length, ℓ_s^+ , which are related through the formula $\omega^+ = 2/\ell_s^{+2}$. Past studies [7, 9] have identified the onset of the VHF regime for forcing frequencies in excess of $\omega^+ > 0.04$, corresponding to a Stokes length of $\ell_s^+ \lesssim 7$. Under these condi-

tions, the Stokes boundary-layer is confined to the viscous sub-layer and is governed by Womersley's laminar solution [12], whereas turbulence statistics appear "frozen" and collapse on top of their non-pulsatile counterpart. Whilst the characteristic behaviours of the CD-VHF regime have been widely reported in the context of pulsatile smooth-wall pipe flow, their applicability in the presence of surface roughness remains unclear.

The principal effect of surface roughness is to cause a downward shift in the mean velocity profile, relative to the smooth-wall case. The rise in momentum deficit is quantified via the roughness function, ΔU^+ , which appears as an additive constant in the log-law. The magnitude of ΔU^+ is known to be a function of the characteristic roughness height and the roughness topography. For example, the sensitivity of ΔU^+ to the amplitude and wavelength of three-dimensional sinusoidal roughness has been systematically demonstrated for non-pulsatile rough-wall pipe flows [1]. Related work has also compared the relative magnitude of roughness-induced and turbulence-induced stresses for the same sinusoidal roughness topographies under non-pulsatile conditions [2] based on a triple decomposition of the instantaneous flow field using a double-averaging (DA) framework [8]. Such an averaging framework can be naturally extended to pulsating rough-wall flows by absorbing temporal phase-averaging techniques [10] into the DA methodology with the aim of isolating the pulsation-induced, roughness-induced and turbulence-induced fluctuations.

To recap, whilst the flow physics of smooth-wall pulsating pipe flow and rough-wall non-pulsating pipe flow have been investigated in substantial separate detail, studies that focus on their combined effect remain rare. As a result, many fluid dynamic properties of pulsatile rough-wall turbulent pipe flows are unclear. For example, the relative magnitude of pulsation-induced, roughness-induced and turbulence-induced stresses in the context of the CD-VHF regime have yet to be considered in detail.

Objectives of the present study

The principal interest here is to obtain a statistical description of a pulsatile rough-wall turbulent pipe flow in the CD-VHF regime in order to draw a direct comparison against its non-pulsatile counterpart. To this end, the objectives of this study are: (i) establish an averaging framework suitable for the decomposition of pulsatile rough-wall turbulent pipe flows; (ii) evaluate and compare the relative magnitudes of the roughness-induced, pulsation-induced and turbulence-induced stresses across a set of systematically varied roughness topographies and (iii) identify any key differences between the statistical descriptions of the pulsatile and non-pulsatile rough-wall pipe flow configurations. To the best of authors' knowledge, points (i)-(iii) remain unaddressed in the literature.

Computational setup and simulation parameters

In this work, data from a DNS was used to study incompressible pulsatile turbulent flow through a pipe roughened with three-dimensional sinusoidal elements. A body-fitted mesh was used to explicitly resolve the rough-walls where impermeable, no-

slip boundary conditions were applied. A periodic boundary condition was applied to the ends of the pipe. The Navier-Stokes and continuity equations were solved in Cartesian coordinates on an “O-grid” mesh using code CDP [4]. Further details can be found in past studies related to the current work [1, 2].

Throughout this study, the cylindrical velocity components $u_i = (u_x, u_r, u_\theta)$ are aligned along their respective axial (x), radial (r) and azimuthal (θ) coordinates. The pipe has a length of $L_x = 2\pi R_0$ where R_0 is the mean pipe radius. All simulations were conducted at a nominal friction Reynolds number of $Re_\tau = 540$. The maximum viscous-scaled mean grid spacings at the wall in the axial (Δx_w^+), radial (Δr_w^+) and azimuthal ($\Delta \theta_w^+$) direction are 4.1, 0.15 and 4.0, respectively.

The roughness topography follows the cosine distribution

$$R(x, \theta) - R_0 = h \cos\left(\frac{2\pi x}{\lambda_x}\right) \cos\left(\frac{2\pi R_0 \theta}{\lambda_\theta}\right) \quad (2)$$

where h is the roughness semi-amplitude and $(\lambda_x, \lambda_\theta)$ are the axial-azimuthal wavelengths. This study focuses on isotropic roughness elements, i.e. $\lambda_x = \lambda_\theta = \lambda$, which were geometrically scaled to a common aspect ratio, h/λ . In total, three roughness topographies were considered — details are listed in table 1.

Pulsation is achieved by imposing a time-varying axial pressure gradient, $\Pi(t)$, which can be written as

$$\Pi(t) = -\Pi_0 [1 + A \cos(\omega t)] \quad (3)$$

where Π_0 is the constant mean axial pressure gradient and where A and ω are the amplitude and frequency of the oscillatory pressure gradient component. All simulations were performed with an amplitude ratio $\beta = 0.06$ and a forcing frequency of $\omega^+ = 0.0582$, giving a Stokes length of $l_s^+ = 2.42$.

Quadruple decomposition of instantaneous flow-field

Considering the doubly-periodicity of the roughness topography (equation 2) and time-harmonic pressure gradient (equation 3), any instantaneous field variable, say f , can be phase-averaged (PA) twice in space and once in time. Temporal phase, ϕ_t , and axial-azimuthal phase, (ϕ_x, ϕ_θ) , are defined here as

$$(\phi_x, \phi_\theta, \phi_t) \equiv \left[\left(\frac{x}{\lambda_x}, \frac{\theta}{\lambda_\theta}, \frac{t}{\mathcal{T}} \right) \bmod 1 \right] \quad (4)$$

where \mathcal{T} is the cycle period and mod is the modulo operator.

A PA quantity, $\langle f \rangle$, is defined here as

$$\langle f \rangle \equiv \lim_{N \rightarrow \infty} \frac{1}{N} \frac{1}{k_x} \frac{1}{k_\theta} \sum_{n=0}^{N-1} \sum_{p=0}^{k_x-1} \sum_{q=0}^{k_\theta-1} f(x'', r, \theta'', t'') \quad (5)$$

where N is the number of pulsation cycles, (k_x, k_θ) is the axial-azimuthal wavenumber pair and superscript double-prime denotes phase-shifted coordinates, i.e. $(x'', \theta'', t'') = (x + p\lambda_x, \theta + q\lambda_\theta, t + n\mathcal{T})$. All PA quantities reported in this work were computed using a sampling period of eight pulsation cycles ($N = 8$) with twenty evenly spaced points per cycle.

A global-averaged (GA) quantity, \bar{f} , is obtained by integrating the PA (equation 5) with respect to spatial-temporal phase

$$\bar{f}(r) \equiv \frac{1}{\mathcal{T}} \frac{1}{\lambda_x} \frac{1}{\lambda_\theta} \int_0^{\mathcal{T}} \int_0^{\lambda_x} \int_0^{\lambda_\theta} \langle f \rangle(\phi_x, r, \phi_\theta, \phi_t) d\phi_\theta d\phi_x d\phi_t \quad (6)$$

The difference between the PA (equation 5) and the GA (equation 6) defines the total phase-averaged fluctuation, \tilde{f} , as

$$\tilde{f}(\phi_x, r, \phi_\theta, \phi_t) \equiv \langle f \rangle(\phi_x, r, \phi_\theta, \phi_t) - \bar{f}(r) \quad (7)$$

which contains the combined effect of the pulsation-induced (PI) and roughness-induced (RI) fluctuations.

The unsteady PI fluctuation, \hat{f} , is isolated by integrating equation 7 with respect to axial-azimuthal phase

$$\hat{f}(r, \phi_t) \equiv \frac{1}{\lambda_x} \frac{1}{\lambda_\theta} \int_0^{\lambda_x} \int_0^{\lambda_\theta} \tilde{f}(\phi_x, r, \phi_\theta, \phi_t) d\phi_\theta d\phi_x \quad (8)$$

Similarly, the steady RI fluctuation, \tilde{f} , is isolated by integrating equation 7 with respect to temporal phase

$$\tilde{f}(\phi_x, r, \phi_\theta) \equiv \frac{1}{\mathcal{T}} \int_0^{\mathcal{T}} \tilde{f}(\phi_x, r, \phi_\theta, \phi_t) d\phi_t \quad (9)$$

Taking equations 5-9 into consideration, the quadruple decomposition of instantaneous axial velocity, u_x , can be written as

$$u_x(\mathbf{x}, t) = \bar{u}_x(r) + \tilde{u}_x(\mathbf{x}) + \hat{u}_x(r, t) + u'_x(\mathbf{x}, t) \quad (10)$$

where $u'_x(\mathbf{x}, t)$ denotes the stochastic fluctuation. In the absence of roughness, i.e. $\tilde{u}_i(\mathbf{x}) \equiv 0$, the quadruple decomposition 10 reduces to the original triple decomposition devised to analyse pulsatile smooth-wall turbulent flow [10].

The quadruple decomposition of instantaneous axial velocity for surface $h_{40}\lambda_{283}$ at an azimuthal-temporal phase of $(\phi_\theta, \phi_t) = (0, 0.25)$ is shown in figure 1. Some initial observations based on this data include: (i) The GA component, \bar{u}_x , is, as expected, inhomogeneous in the wall-normal direction; (ii) beyond a height of approximately four semi-amplitudes ($y/h \gtrsim 4$), the magnitude of the RI fluctuation, \tilde{u}_x , becomes negligible — corresponding to the upper edge of the roughness layer; (iii) within closer proximity of the roughness crests ($y/h \lesssim 1$), \tilde{u}_x becomes predominantly negative — reflecting the deficit of axial momentum in this region; (iv) the PI fluctuation, \hat{u}_x , is comprised of a thin shear-layer in the near-wall region ($y/h \ll 1$) and “plug-flow” in the outer layer and (v) the stochastic fluctuation, u'_x , reveals inclined and elongated structures synonymous with wall-bounded turbulence. Whilst the basic structure of pulsatile rough-wall pipe flow can be drawn from figure 1, a better understanding can be gained by analysing statistical quantities.

Quadruple decomposition of GA axial velocity statistics

Profiles of GA axial velocity, \bar{u}_x , are shown in figure 2a. The pulsatile and non-pulsatile rough-wall data collapse well in the outer region for each surface and, as a result, the roughness functions, ΔU^+ , are approximately equal (see table 1). Such a collapse is not, however, observed in the near-roughness region. For example, below the roughness crests ($y/h < 1$), the GA axial velocity profiles of the pulsatile data show a consistently lower value than their steady counterpart (see inset panel figure 2a). This observation is in contrast to the non-pulsatile and pulsatile smooth-wall data — which collapses for all wall-normal positions in the CD-VHF regime [7, 9].

Profiles of the RMS RI stress, $\tilde{u}_{x,\text{rms}} = \sqrt{u_x - [\bar{u}_x + \hat{u}_x]^2}$, are shown in figure 2b. Similar to the GA axial velocity profiles shown in figure 2a, the profiles of $\tilde{u}_{x,\text{rms}}$ collapse well in the outer-region. In-line with recent findings of [2], the RI stresses increase with increasing roughness height (h^+) and persist well into the log-law region. For example, at a height of one hundred wall-units ($y^+ = 100$) the RI stress induced by surface $h_{80}\lambda_{565}$ retains 50% of its peak value. The maximum RI stress for the pulsatile and non-pulsatile data occurs just above the roughness crests ($y/h \approx 1$), where the former exhibits a slightly larger magnitude. Below the roughness crests, the RI stress profiles exhibit the same behaviour as the GA axial velocity profiles (figure 2a) whereby the pulsatile stress profiles “peel-off”

Case	k_x	k_θ	h/λ	λ/R_0	R_0/h	h^+	λ^+	k_a^+	k_{rms}^+	ES	ΔU^+	Line
$h_{20}\lambda_{141}$	48	24	0.141	$\pi/12$	27	20.0	141	8.11	10.0	0.36	6.25	(—)
$h_{40}\lambda_{283}$	24	12	0.141	$\pi/6$	14	40.0	283	16.2	20.0	0.36	8.87	(- - -)
$h_{80}\lambda_{565}$	12	8	0.141	$\pi/3$	7	80.0	565	32.4	40.0	0.36	11.83	(⋯⋯)

Table 1: Roughness parameters including: axial-azimuthal wavenumber pair, (k_x, k_θ) ; ratio of roughness semi-amplitude to roughness wavelength, h/λ , roughness wavelength to mean pipe radius, λ/R_0 , and mean pipe radius to roughness semi-amplitude, R_0/h ; viscous-scaled roughness semi-amplitude, h^+ , roughness wavelength, λ^+ , mean absolute roughness height, k_a^+ , root-mean-square roughness height, k_{rms}^+ , and effective slope, ES . The roughness function, ΔU^+ , is also included for each surface.

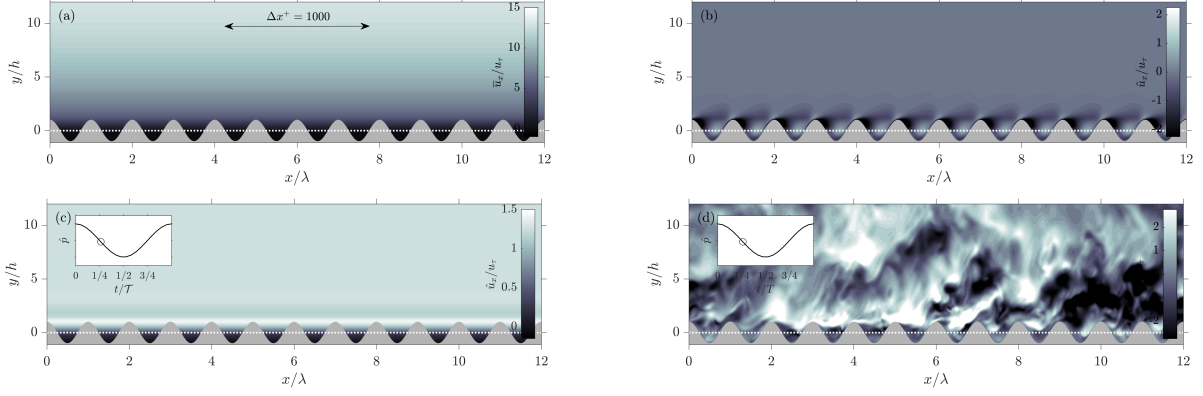


Figure 1: Quadruple decomposition of instantaneous axial velocity, u_x , including the: (a) GA component, \bar{u}_x ; (b) steady RI component, \tilde{u}_x ; (c) unsteady PI component, \hat{u}_x , and (d) the turbulent component, u'_x . Data corresponds to an azimuthal-temporal phase of $(\phi_\theta, \phi_t) = (0, 0.25)$ and has been normalised by the mean friction velocity, u_τ , the roughness semi-amplitude, h , and the roughness wavelength, λ . The height of the mean pipe radius, R_0 , is marked by the horizontal dotted line.

from their non-pulsatile counterpart. The inset panel figure 2b shows profiles of $\tilde{u}_{x,rms}$ plotted against the wall-normal height normalised by the roughness semi-amplitude (y/h). The profiles collapse in the vicinity of the roughness crests ($y/h \approx 1$) and attain a negligible magnitude above a height of approximately four semi-amplitudes ($y/h \gtrsim 4$) — which agrees well with the thickness of the roughness layer shown in figure 1b.

Profiles of the RMS PI stress, $\hat{u}_{x,rms} = \sqrt{(u_x - [\bar{u}_x + \tilde{u}_x])^2}$, are shown in figure 2c. In the outer flow, the smooth- and rough-wall data collapse where the horizontal nature of the stress profile indicates a shear-free “plug-flow” region. The peak value of $\hat{u}_{x,rms}$ approximately coincides with the roughness crests ($y/h \approx 1$) and is invariant with respect to the roughness height (h^+). In addition, for all roughness topographies considered so far, the peak value of $\hat{u}_{x,rms}$ exceeds that of the smooth-wall. It is worth noting that the velocity profile of the smooth-wall Stokes-layer is strictly one-dimensional ($\hat{u}_r = \hat{u}_\theta = 0$), whereas, for the rough-wall configurations, a three-dimensional Stokes-layer occurs. Furthermore, the off-diagonal components of the PI stress tensor, $\hat{u}_i \hat{u}_j$, become non-zero — enabling additional mechanisms of momentum transport throughout the oscillating near-wall layer. Whilst the contributions of the RI shear stress and the Reynolds shear stress to the balance of GA axial momentum are well-documented in the context of non-pulsatile rough-wall flows [5], additional mechanisms must be accounted for in the presence of pulsation. For example, it is anticipated that the wall-normal gradient of the GA PI shear stress, i.e. $-\partial \hat{u}_x \hat{u}_r / \partial x_r$, will influence the mean flow dynamics of pulsatile rough-wall pipe flow in the near-wall region.

Profiles of the RMS Reynolds stress, $u'_{x,rms} = \sqrt{(u_x - \langle u_x \rangle)^2}$, are shown in figure 2d. Similar to the GA profiles of mean velocity (figure 2a) and RMS RI stress (figure 2b), the pulsatile and non-pulsatile data agree well in the outer region — offering support for Townsend’s outer-layer similarity hypoth-

esis [11]. The peak RMS Reynolds stress occurs just above the roughness crests and its magnitude is comparable to that of the non-pulsatile value. In contrast, below the roughness crests ($y/h < 1$) the profiles of $u'_{x,rms}$ exhibit a similar behaviour previously observed in figure 2a and figure 2b, whereby the magnitude of the RMS Reynolds stress in the lower part of the roughness canopies becomes suppressed, relative to the non-pulsatile rough-wall data.

Discussion

Pulsatile rough-wall turbulent pipe flow in the CD-VHF regime has been investigated using DNS at a friction Reynolds number of $Re_\tau = 540$. Using data from an equivalent non-pulsatile dataset at the same friction Reynolds number [1, 2], a direct comparison between the two flow configurations was made. Statistical quantities were computed following a quadruple decomposition of the instantaneous axial velocity (equation 10). Based on an analysis of the GA statistics, the key observations of this study include: (i) excellent collapse in the outer-layer profiles of mean velocity (figure 2a), RMS RI stress (figure 2b) and RMS Reynolds stress (figure 2d) are observed between the non-pulsatile and pulsatile data — amounting to considerable supporting evidence of Townsend’s outer-layer similarity hypothesis for rough-wall pulsatile flow; (ii) the peak value of PI stress is enhanced in the presence of surface roughness (figure 2c) — which we anticipate to be related to the three-dimensionalisation of the rough-wall Stokes-layer and (iii) below the highest roughness crest ($y/h < 1$) the magnitudes of GA mean velocity (figure 2a), RMS RI stress (figure 2b) and RMS Reynolds stress (figure 2d) show consistently lower values than their non-pulsatile counterparts. Considering these differences, future work will focus on the near-roughness region where phase-averaged statistics of the roughness-induced, pulsation-induced and turbulence-induced fluctuations will be examined in detail.

Themes: Turbulence, Computational fluid dynamics, Bound-

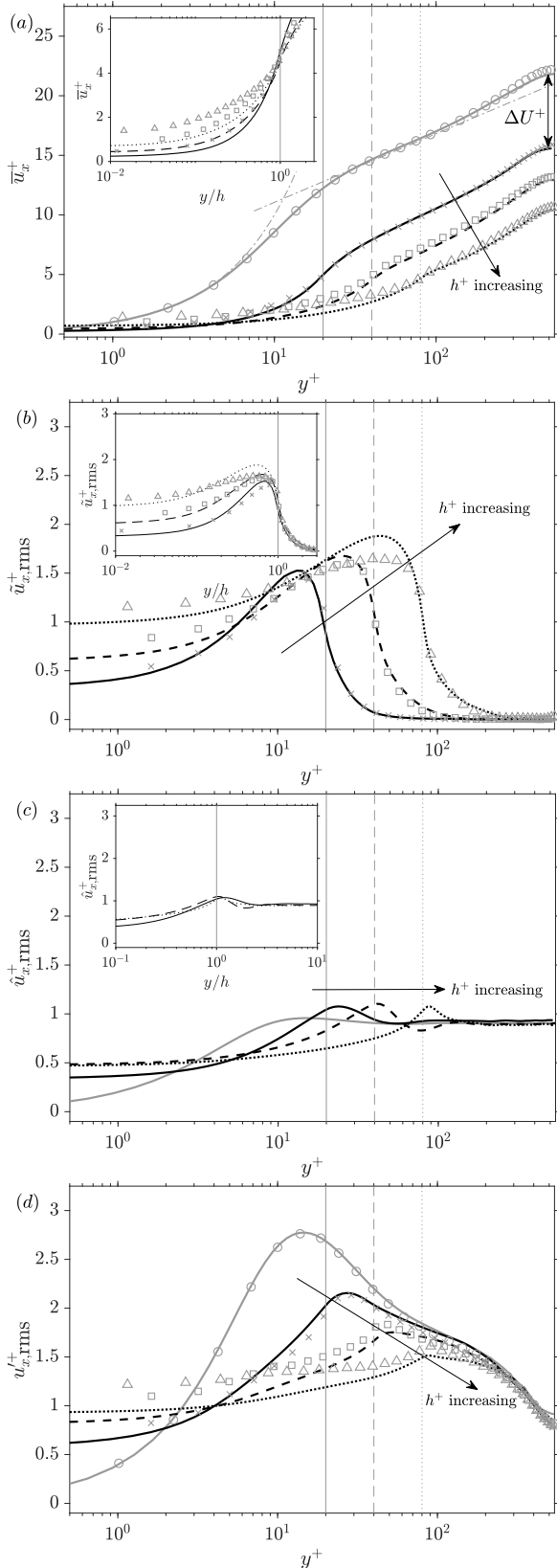


Figure 2: GA axial velocity statistics including: (a) mean velocity profile; (b) RMS RI stress; (c) RMS PI stress and (d) RMS Reynolds stress. Line types for pulsatile rough-wall data are given in table 1. Data for smooth-wall non-pulsatile (\circ), smooth-wall pulsatile (—) and non-pulsatile rough-wall cases $h_{20}\lambda_{141}$ (\times), $h_{40}\lambda_{283}$ (\square) and $h_{80}\lambda_{565}$ (\triangle) from [1, 2] are also included for $Re_\tau = 540$. Vertical lines indicate the roughness crests.

ary layers.

Acknowledgements

This work was supported by the ARC Linkage Project (LP150100233). This research was undertaken with the assistance of resources and services from the National Computational Infrastructure (NCI), which is supported by the Australian Government.

References

- [1] L. Chan, M. MacDonald, D. Chung, N. Hutchins, and A. Ooi. A systematic investigation of roughness height and wavelength in turbulent pipe flow in the transitionally rough regime. *J. Fluid Mech.*, 771:743–777, 2015.
- [2] L. Chan, M. MacDonald, D. Chung, N. Hutchins, and A. Ooi. Secondary motion in turbulent pipe flow with three-dimensional roughness. *J. Fluid Mech.*, 854:5–33, 2018.
- [3] K. A. Flack and M. P. Schultz. Roughness effects on wall-bounded turbulent flows. *Phys. Fluids*, 26(10):101305, 2014.
- [4] F. Ham, K. Mattsson, and G. Iaccarino. Accurate and stable finite volume operators for unstructured flow solvers. *Annual Research Briefs*, pages 243–261, 2006.
- [5] T. O. Jelly and A. Busse. Reynolds and dispersive shear stress contributions above highly skewed roughness. *J. Fluid Mech.*, 852:710–724, 2018.
- [6] C. Lodahl, B. M. Sumer, and J. Fredsøe. Turbulent combined oscillatory flow and current in a pipe. *J. Fluid Mech.*, 373:313–348, 1998.
- [7] M. Manna, A. Vacca, and R. Verzicco. Pulsating pipe flow with large-amplitude oscillations in the very high frequency regime. Part 1. Time-averaged analysis. *J. Fluid Mech.*, 700:246–282, 2012.
- [8] V. Nikora, I. McEwan, S. McLean, S. Coleman, D. Pokrajac, and R. Walters. Double-averaging concept for roughbed open-channel and overland flows: Theoretical background. *J. Hydraul. Eng.*, 133(8):873–883, 2007.
- [9] P. Papadopoulos and A. Vouros. Pulsating turbulent pipe flow in the current dominated regime at high and very-high frequencies. *Int. J. Heat Fluid Fl.*, 58:54–67, 2016.
- [10] W. Reynolds and A. Hussain. The mechanics of an organized wave in turbulent shear flow. Part 3. Theoretical models and comparisons with experiments. *J. Fluid Mech.*, 54(2):263–288, 1972.
- [11] A. A. Townsend. *The Structure of Turbulent Shear Flow*. Cambridge University Press, 2nd edition, 1976.
- [12] J. R. Womersley. Method for the calculation of velocity, rate of flow and viscous drag in arteries when the pressure gradient is known. *J. Physiol.*, 127(3):553–563, 1955.
- [13] D. Xu, S. Warnecke, B. Song, X. Ma, and B. Hof. Transition to turbulence in pulsating pipe flow. *J. Fluid Mech.*, 831:418–432, 2017.